**PAPER • OPEN ACCESS**

# Crossover from ballistic to diffusive thermal transport in suspended graphene membranes

View the article online for updates and enhancements.

# IOP ebooks™

Bringing you innovative digital publishing with leading voices to create your essential collection of books in STEM research.

Start exploring the collection - download the first chapter of every title for free.

## 2D Materials

**PAPER**

# Crossover from ballistic to diffusive thermal transport in suspended graphene membranes

A El Sachat[1,4] , F Köenemann[2], F Menges[2,5], E Del Corro[1], J A Garrido[1,3], C M Sotomayor Torres[1,3], F Alzina[1] and B Gotsmann[2]

[1] Catalan Institute of Nanoscience and Nanotechnology (ICN2), CSIC and BIST, Campus UAB, Bellaterra, 08193 Barcelona, Spain
[2] IBM Research - Zurich, Säumerstrasse 4, 8803 Rüchlikon, Switzerland
[3] ICREA, Passeig Lluis Companys 23, 08010 Barcelona, Spain
[4] Present address: Facultad de Ciencias, Departamento de Física de la Materia Condensada and Condensed Matter. Physics Center (IFIMAC), C/ Francisco Tomás y Valiente 7, Universidad Autónoma de Madrid, 28049, Madrid, Spain
[5] Present address: Department of Physics, University of Colorado, CO-80309, Boulder, United States of America

E-mail: alexandros.elsachat@uam.es

## Abstract

We report heat transport measurements on suspended single-layer graphene disks with radius of 150–1600 nm using a high-vacuum scanning thermal microscope. The results of this study revealed a radius-dependent thermal contact resistance between tip and graphene, with values between 1.15 and $1.52 \times 10^8 \, \text{KW}^{-1}$. The observed scaling of thermal resistance with radius is interpreted in terms of ballistic phonon transport in suspended graphene discs with radius smaller than 775 nm. In larger suspended graphene discs (radius >775 nm), the thermal resistance increases with radius, which is attributed to in-plane heat transport being limited by phonon–phonon resistive scattering processes, which resulted in a transition from ballistic to diffusive thermal transport. In addition, by simultaneously mapping topography and steady-state heat flux signals between a self-heated scanning probe sensor and graphene with 17 nm thermal spatial resolution, we demonstrated that the surface quality of the suspended graphene and its connectivity with the Si/SiO$_2$ substrate play a determining role in thermal transport. Our approach allows the investigation of heat transport in suspended graphene at sub-micrometre length scales and overcomes major limitations of conventional experimental methods usually caused by extrinsic thermal contact resistances, assumptions on the value of the graphene's optical absorbance and limited thermal spatial resolution.

## 1. Introduction

Graphene is a subject of intense research because of its unique electronic and thermal transport behavior that makes it attractive for large-scale integration in future nanoelectronic devices. In particular, graphene's high room-temperature carrier mobility [1] and high thermal conductivity [2] makes it a promising candidate for thermal management in nanoelectronic circuits [3, 4]. However, engineering graphene in sub-micrometre size devices requires the understanding of heat dissipation at the nanoscale, which is mainly dominated by a ballistic rather than a diffusive mechanism [2, 5–8]. Despite the enormous progress over the last few years, the understanding of the fundamentals of heat transport in graphene at sub-micrometre scale still remains an unresolved challenge for several reasons. To a certain extent, the lack of understanding arises from technical limitations imposed by the experimental methods available to study heat transport at the nanoscale. For instance, current experimental techniques, including Raman spectroscopy [9–14] and electro-thermal methods [15–22], proved to be insufficient for thermal characterization in nanometer-scale samples. Moreover, both methods have shown contradictive results with large uncertainties. In the opto-thermal techniques, in addition to the uncertainties caused by the value of the graphene's optical absorbance and the limited temperature sensitivity, the relatively

large size of the focused laser spot limits the heat transport studies to micrometre-scale samples. In the electro-thermal methods besides the difficult sample preparation, the high extrinsic thermal contact resistance (graphene/electrode contacts) in submicron samples complicates the experimental data interpretation and eventually leads to ambiguous results. Recently Nika *et al* [23, 24] summarized the current available experimental heat transport results in graphene obtained from the aforementioned methods, emphasizing the wide discrepancies and the issue of accuracy. Consequently, these technique-related restrictions limit the understanding of ballistic thermal transport in graphene, which requires thermal spatial resolution below the phonons mean free path (MFP).

Apart from the difficulties of the measurement methods, CVD graphene samples often show substrate-induced surface corrugations, such as ripples or wrinkles, which are formed during the CVD growth and retained after the transfer [25]. The origin of these surface corrugations are related to the morphology of the substrate on which the graphene layer was grown. Calado *et al* [26] suggested that the water drainage between graphene and substrate during the transfer process plays an important role in wrinkle formation. In addition, it has been shown that the formation of wrinkles is particularly related to the adhesion and the magnitude of strain between graphene and substrate [27]. Although the formation mechanisms responsible for such surface corrugations in graphene has been extensively discussed elsewhere [25], the effect of this kind of surface corrugations on thermal transport remains almost unknown [28]. Furthermore, CVD graphene samples often suffer from high surface contamination from polymer residue, which usually formed during the transfer process [29–31], and may affect graphene's intrinsic electronic and thermal properties [25]. For instance, low quality suspended graphene samples exhibit thermal resistance or thermal conductivity that differ from the intrinsic value predicted for clean suspended graphene [18, 32]. Although several experiments have been developed over the last decade to study thermal transport in CVD suspended monolayer graphene [1, 11, 20, 32, 33], the effect of graphene's surface contamination on the heat transport results is rarely discussed [32]. Therefore experimental heat transport data of CVD suspended graphene with defined morphology and high thermal spatial resolution are still lacking.

In this work we address the aforementioned challenges by studying thermal transport in suspended monolayer graphene in a high-vacuum ($10^{-6}$ mbar) scanning thermal microscope, which directly enables quantitative heat flux measurements and thermal mapping with spatial resolution down to few-nanometre. The tip of the scanning thermal microscope effectively acts as a point-like heat source. More details about the experimental setup can be found

elsewhere [34]. By measuring topography and steady-state heat flux signals between a self-heated scanning probe sensor and suspended graphene micro-discs of different radius, we quantify the in-plane heat transport, providing in parallel a valuable information regarding the surface quality and morphology of the graphene discs. Therefore, we attribute the differences in the measured thermal resistance only to variations in the sample radius and not to the additional scattering that resulted from surface contamination or deformation.

## 2. Materials and methods

### 2.1. Fabrication
Graphene was grown by chemical vapor deposition on a $4.5 \times 7$ cm$^2$ copper foil previously electropolished, followed by a one hour annealing step at 1015 °C, like described elsewhere [35]. For growing times of 15 min at 12 mbar (1000 sccm Ar/200 sccm H2/2 sccm CH4) the graphene samples consist of a closed monolayer with a low density of second nucleation grains, as revealed by scanning electron microscopy. Graphene samples are transferred to the final substrate (Si/SiO$_2$) by a wet chemical method using poly (methyl methacrylate) as sacrificial polymer and iron chloride for the cooper etching. The graphene samples are characterized by Raman spectroscopy before and after the transfer procedure to prove that the quality of the graphene is preserved during the process. The Raman spectra (see also figure S2 in the Supporting information (SI) (stacks.iop.org/TDM/6/10.1088/2053-1583/ab097d/mmedia)) reveal a monolayer graphene sheet free of structural defects [36].

### 2.2. Thermal analysis
To quantify the local tip-sample thermal resistance, a self-heated scanning thermal microscope cantilever was used in active mode operation to measure the heat flux variations caused by the difference in tip-sample temperature. The measured heat flux signals depend on both the temperature difference and the tip-sample thermal resistance ($R_{ts}$) and is equal to $\dot{Q}_{ts} = (T_t - T_s)/R_{ts}$. The temperature of the integrated heater/sensor ($T_t = 180$ °C), was controlled by applying a DC current to the resistive silicon scanning probe cantilever [37]. The temperature of the sample was kept at a room temperature ($T_s = RT = 20$ °C). The thermal resistance of the cantilever was measured from the voltage drop across the heater/sensor while the $R_{ts}$ was extracted by measuring the change of the thermal resistance in contact ($R_{th,in}$) and out of contact ($R_{th,out}$), $R_{ts} = (R_{th,in}^{-1} - R_{th,out}^{-1})^{-1}$. More details regarding the probe calibration and the quantification of the $R_{ts}$ are given elsewhere [34]. Taking into account the thermal resistive components at the tip-graphene contacts, the $R_{ts}$ can be described by a series of resistors, as follows:
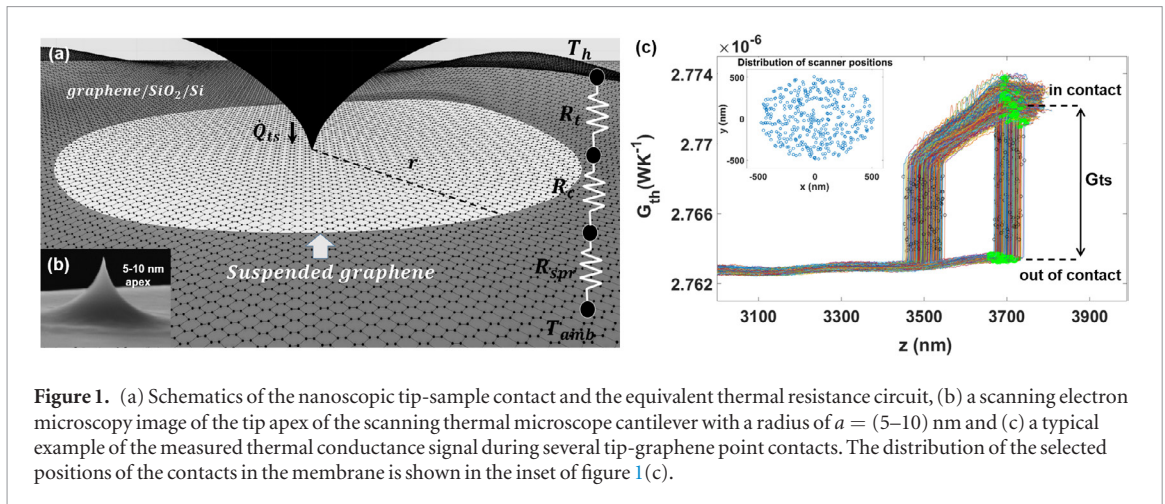
**Figure 1.** (a) Schematics of the nanoscopic tip-sample contact and the equivalent thermal resistance circuit, (b) a scanning electron microscopy image of the tip apex of the scanning thermal microscope cantilever with a radius of $a = (5–10)$ nm and (c) a typical example of the measured thermal conductance signal during several tip-graphene point contacts. The distribution of the selected positions of the contacts in the membrane is shown in the inset of figure 1(c).

$$R_{ts} = R_t + R_c + R_{spr} \qquad (1)$$

where $R_t$ is the thermal resistance of the tip, $R_c$ is the thermal interface resistance between the tip and graphene (thermal contact resistance) and $R_{spr}$ is the thermal spreading resistance in the graphene membrane and into the substrate. Note, that this equation implies a diffusive transport in the graphene sample. If the transport is ballistic in the graphene membrane, then the thermal contact between tip and graphene is a part of the ballistic transport problem and $R_c$ cannot be written as a summand for $R_{ts}$ independent from $R_{spr}$. Figures 1(a) and (b) display schematics of the nanoscopic tip-sample contact, the equivalent thermal resistance circuit and a scanning electron microscopy image of the tip apex with radius of $a = (5–10)$ nm. In figure 1(c) is shown a typical example of the measured thermal conductance signal when the tip is brought in and out of contact with a suspended graphene membrane at different positions.
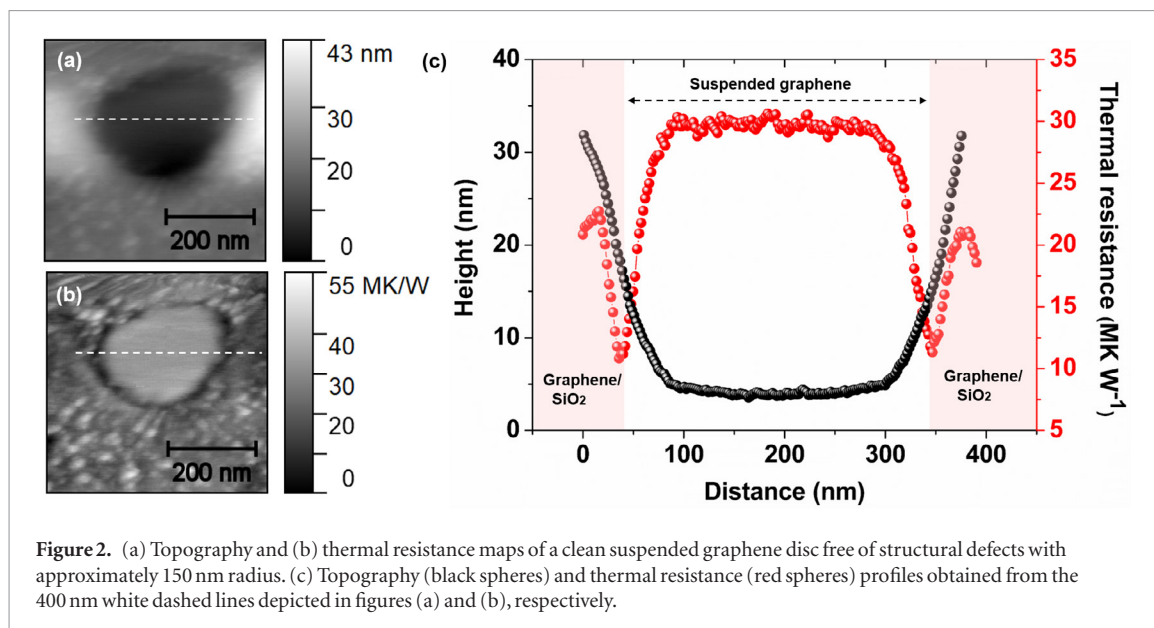
## 3. Results and discussion

First, we obtain topography and thermal resistance maps of several suspended graphene disks with radius between 150 nm and 1600 nm by simultaneous measuring the local variations in topography and tip-sample thermal resistance. Figures 2(a) and (b) show typical examples of the topography and the corresponding thermal resistance image of a suspended graphene discs with 150 nm radius. The topography image in figure 2(a) shows a clean graphene surface without defects and polymer residue. However, the graphene membrane exhibits pronounced out-of-plane deformation with a height of approximately 25 nm. This kind of out-of-plane deformation is related to the interaction between the substrate and the suspended graphene and usually arises from a tensile strain that is created during the fabrication process [29, 38]. Similarly, nanometre-sized deformations in graphene have been observed in previous studies [25, 30, 31, 39].

The thermal resistance map (figure 2(b)) shows clear differences between supported and suspended graphene areas with a spatial resolution of 17 nm. The estimation of the thermal spatial resolution was extracted by comparing topography and thermal resistance data, as described in detail in figure S5 (see SI). The brighter homogeneous contrast in the central part of the thermal resistance image (figure 2(b)) indicates decreased heat flow and an increased tip-sample thermal resistance. We attribute this behavior to the change in both $R_c$ and $R_{spr}$ when the tip is moving from the suspended graphene (brighter region) to graphene-SiO$_2$ contacts. The relative variations of the thermal resistance and topography signals between tip-graphene-SiO$_2$ and tip-graphene contacts can be directly observed in the profiles of figure 2(c) (obtained from the line scans shown in figures 2(a) and (b)). Topography-related resistance modulations are visible in the graphene-SiO$_2$ regions and at the edges of the suspended graphene due to the relatively large variations of the tip-sample contact geometry. However, in the suspended graphene disc, we observe a rather constant, homogeneous thermal resistance signal due to the flat surface topography. In particular, the topography variations in the suspended part are smaller than ~1 nm and the corresponding thermal resistance signal is constant with error less than 1% of the average value. This result indicates a clear distinguish of the two measured signal levels in the transferred graphene and ballistic thermal transport. In addition, in the SI (figure S3), we show that for relatively large graphene membranes (e.g. $r \sim 1.6$ $\mu$m), a thermal resistance gradient appears as the tip-membrane contact moves toward the edge of the membrane. The thermal resistance decrease, which is not only topography related as in the case of the graphene membrane with $r \sim 150$ nm, might be related to the dominance of the diffusive transport.

Note that in few graphene membranes wrinkles or contaminated surface were visible both in the supported and the suspended graphene. In figure S4 (see SI), we show examples of graphene membranes with wrinkles, defects and contaminated surface from polymer residue that are detected by our scanning thermal microscope. In particular, the thermal resist-

**Figure 2.** (a) Topography and (b) thermal resistance maps of a clean suspended graphene disc free of structural defects with approximately 150 nm radius. (c) Topography (black spheres) and thermal resistance (red spheres) profiles obtained from the 400 nm white dashed lines depicted in figures (a) and (b), respectively.

ance profile of figure S4(g) shows a 35% decrease of the thermal resistance due to a wrinkle that formed in a suspended graphene membrane (see figures S4(c) and (d)). Although this decrease might be attributed to the contact area variations when the tip is moving from a lower height level towards the wrinkle, by comparing the cross sectional topography and thermal resistance profiles of figure S4(g), we observe a smooth topography change (~3 nm) from the suspended part towards the wrinkle and a relatively large decrease of the thermal resistance signal. Note that previous topography changes of approximately similar height in a suspended graphene with absence of wrinkle did not show similar magnitude change of the thermal resistance signal. Therefore, the decrease of the thermal resistance in the wrinkle most likely is not related to the geometrical change of the contact area only. The identification of such surface corrugations is a clear demonstration of the general idea of our approach, which aims to study heat transport in graphene at submicrometre samples by simultaneously analyzing the surface topography of the graphene, and show that it is possible to correlate changes in the thermal resistance to the presence of such surface corrugations in the graphene surface.

Furthermore, in figures S5(a) and (b) in the SI, we show the topography and the corresponding thermal resistance map of a suspended graphene disc with 550 nm radius, where the thermal contrast between suspended and supported graphene has been changed. The darker contrast (suspended graphene) in the thermal resistance image (figure S5(b)) indicates increased heat flow and a lower thermal resistance. Note that this is the first indication of the increased in plane heat dissipation with increasing radius. Similarly, from the thermal resistance profile (figure S5(c)), we observe topography-related resistance modulations in graphene-$SiO_2$ regions and a homogeneous thermal resistance signal in the suspended graphene.

In order to quantify the variation of the thermal resistance with the size of the suspended graphene, we have studied a set of samples with varying radius. For this purpose, we obtain the average $R_{ts}$ for each suspended graphene disc by monitoring the heat flux signals transferred from the tip to several nanoscopic contacts of the graphene surface. Figure 3(a) displays the average thermal resistance, $R_{ts}$, as a function of the radius of the graphene discs. Note that the imaging of the surface topography of all the membranes was performed prior to these measurements in order to determine the surface quality and morphology of the transferred suspended graphene. Furthermore, by measuring the deflection of the cantilever during the approach-retract process, we estimated the mean value of the adhesion force for each graphene disc (figure 3(b)). A variation in the adhesion force points to a variation of the tip-sample contact through either a variation of sample compliance or, more frequently, a contamination of the tip. A constant adhesion force is therefore an indication of preserved integrity of the tip during the experiments. Therefore, in all the tip-graphene contacts we ensured that the applied contacting force, thus the thermal contact was similar. Graphene membranes that showed higher or lower average adhesion force and correspondingly higher or lower average thermal conductance have been excluded from the analysis. Note also that polymer residues (or defects) might potentially increase the thermal resistance of the graphene membranes. Therefore, it was essential to compare thermal transport data derived from clean graphene membranes with similar morphology.

Figure 3(a) shows an approximately linear thermal resistance decrease with increasing graphene radius until 775 nm. The decrease of $R_{ts}$ with increasing radius suggests an increase of the in-plane heat dissipation in the suspended graphene. On the other hand, in graphene discs with a radius larger than 775 nm we found that the thermal resistance increases with
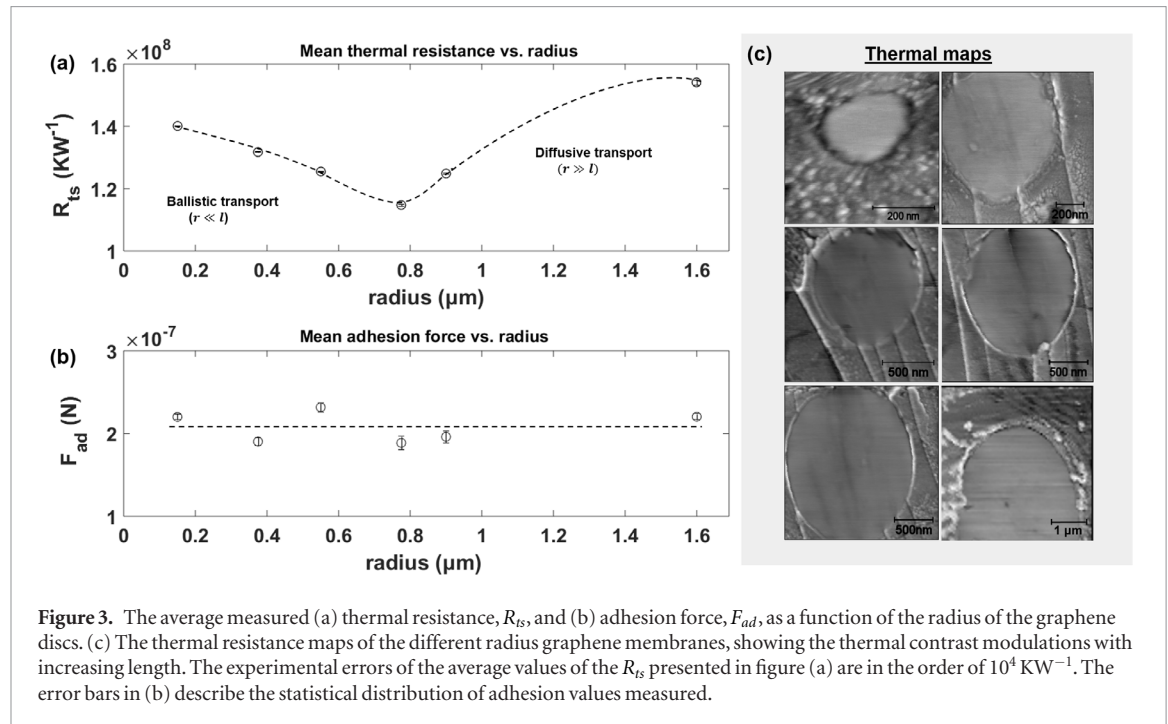
**Figure 3.** The average measured (a) thermal resistance, $R_{ts}$, and (b) adhesion force, $F_{ad}$, as a function of the radius of the graphene discs. (c) The thermal resistance maps of the different radius graphene membranes, showing the thermal contrast modulations with increasing length. The experimental errors of the average values of the $R_{ts}$ presented in figure (a) are in the order of $10^4 \, \mathrm{KW^{-1}}$. The error bars in (b) describe the statistical distribution of adhesion values measured.

increasing radius. A second set of experimental data acquired with a different scanning thermal microscope cantilever, confirmed the increase of the thermal resistance with graphene radius after 775 nm (see figure S7 in the SI). It is worth mentioning also that the experimental trend is consistent with the absolute thermal contrast changes with increasing graphene radius, as shown in the thermal images in figure 3(c). In particular, by increasing the radius of the graphene discs from 150 nm to 775 nm the absolute thermal contrast becomes darker. Then, by increasing further the radius of the graphene discs (from 775 nm to 1.6 µm), the thermal contrast becomes brighter and correspondingly the thermal resistance is increasing.

Next, we analyze the experimentally observed trend of the radius–dependent thermal resistance. As the thermal resistance $R_{ts}$ is a sum of different components, we need to identify the components responsible for the observed variation. The thermal resistance of the tip $R_t$ can be safely assumed constant. The heat spreading into the silicon substrate in the region in which the graphene is supported is a function of the membrane dimension. Using a heat diffusion equation in the cylindrical coordinates, we calculate $R_{sup}$ as follows [11]:

$$R_{sup} = \frac{1}{2\pi r(\sqrt{gtk_s})} \frac{K_o(Z_r)}{K_1(Z_r)} \qquad (2)$$

where $g = 8.34 \times 10^7 \, \mathrm{W\,m^{-2}\,K^{-1}}$ is the total interface thermal conductance per unit area between graphene and $SiO_2$ [14, 40], $k_s = 370 \, \mathrm{W\,m^{-1}\,K^{-1}}$ is the thermal conductivity of the supported graphene, $t = 0.335 \, \mathrm{nm}$ is the thickness of graphene [41], $Z_r = r(g/k_s t)^{1/2}$ [11] and $K_0$, $K_1$ are the zero and the first order Bessel functions, respectively. From the equation (2) we find that as the graphene's disk radius increases, $R_{sup}$

exponentially decreases and that for relatively large suspended graphene disks, $R_{sup}$ becomes negligible. In particular, by increasing the graphene radius from 150 to 775 nm the $R_{sup}$ is decreasing from $2.9 \times 10^5$ to $6.2 \times 10^4 \, \mathrm{KW^{-1}}$. The exact values of $R_{sup}$ as a function of different graphene lengths are given in the SI, in Figure S8. Although the effect of the $R_{sup}$ in the measured $R_{ts}$ might be considerable, from the experimental data in figure 3(a), we can see that the magnitude change of the measured $R_{ts}$ in graphene discs with radius between 150 and 775 nm is almost two order of magnitude larger than the decrease of the $R_{sup}$ for the same length range. Therefore, the contribution of $R_{sup}$ to the thermal resistance of the sample $R_{spr}$ and to the total thermal resistance $R_{ts}$ is negligible. This leaves us with the thermal resistance of the suspended part of the graphene as the main candidate for the observed dependence on flake radius.

Next, we consider both ballistic and diffusive thermal transport in the suspended graphene. The average MFP of thermal phonons in graphene estimated from measurements ranges from 250 nm [22] to 800 nm [3]. Regarding calculated values, single-phonon excitations show typical MFP of about 1 µm [42]. Although an increase of two orders of magnitude was calculated for collective excitations [43], it has been recently shown that the MFP recovers the values similar to the single-phonon approximation, when four-phonon scattering processes are introduced [44]. Since the radius ($r$) of the measured graphene discs are in the range of the expected MFPs, we can expect deviations from a diffusive thermal transport and ballistic transport needs to be considered.

Taking into account the sample geometry, we define a 'ballistic channel length' equal to the distance between the tip-graphene point contact and the

supported graphene. Thus, by approaching the tip in the center of the graphene discs, the ballistic channel length becomes equal to the radius of the disc and a symmetrical in-plane propagation of ballistic phonons from the tip apex to the supported graphene is expected. In this transport regime, the ballistic thermal resistance ($R_b$) is modeled as a constant [45]:

$$R_b \propto \frac{1}{A \sum_\lambda C_\lambda \, |v_{x,\lambda}| \, \alpha_\lambda} \tag{3}$$

where $A$ is the cross-section of the heated area, $\lambda$ is the number of phonon modes, $C_\lambda$ is the volumetric specific heat contribution, $v_{x,\lambda}$ is the group velocity along the temperature gradient for the phonon mode $\lambda$ and $\alpha_\lambda$ is the phonon transmission coefficient across the interfaces between the suspended and supported graphene. As the transport regime becomes purely ballistic, the temperature jump at the interface between suspended and supported graphene increases and the absolute temperature gradient inside the suspended graphene decreases. Note that the ballistic resistance in this case is essentially the intrinsic thermal resistance of graphene. On the contrary, in the purely diffusive regime the thermal resistance increases with increasing radius as:

$$R_d = \int_a^r \frac{dr}{2\pi r t \kappa} = \frac{\ln \frac{r}{a}}{2\pi t \kappa} \tag{4}$$

where $\alpha$ is the radius of the heated area, $t$ is the thickness of graphene and $\kappa$ the thermal conductivity in the Fourier law. The phenomenological transmission coefficient in equation (3), $\left( \alpha_\lambda = 1 + \frac{\ln \frac{r}{a}}{l} \right)^{-1}$ [45], introduces the probability of heat carriers undergo scattering. This results in the smoothing of the otherwise abrupt transition between the length dependent diffusive resistance and the pure ballistic limit.

Considering the high surface quality of the suspended graphene micro-discs, thus the absence of phonon scattering on polymer residue and defects, this result suggests a ballistic phonon transport up to 775 nm (ballistic channel length) approximately and a radius-dependent thermal resistance. The observed increased in-plane heat dissipation with increasing graphene lateral size can be attributed to the increase population of in-plane ballistic phonons at stationary non-equilibrium conditions. In other words, as the radius increases, more low-frequency acoustic phonons are excited and contribute to thermal conduction, resulting in a length-dependent behavior. Similarly, it has been shown, that heat transport in suspended graphene can be conducted from ballistic phonons [46] and quasi-ballistic heat flow effects should be considered in graphene samples shorter than 1 μm [32, 47]. The importance of the low-frequency acoustic phonons on heat transport with increasing graphene size has been emphasized also in several theoretical works [48, 49].

We point out that in our experimental configuration the size of the heat source is more than one order of magnitude smaller than the average MFP of the phonons in graphene, thus it was essential to consider in the analysis a model that explains the heat transport results in the ballistic transport regime. According to previous reports [46, 50, 51] the thermal resistance depends on the Knudsen number $K_n = l/a$. In the ballistic regime ($K_n \gg 1$) an increase in the thermal resistance is expected due to the additional ballistic resistance. This trend has been observed in our experimental data in figure 3(a) (see also SI, figure S7), where it is shown that graphene discs with a radius smaller than 775 nm exhibit increased $R_{ts}$ due to the increase of the ballistic resistance.

In the suspended graphene discs with a radius comparable with the average MFP of phonons ($r \sim l$), the thermal transport regime consists of both ballistic and diffusive features. In such cases the intrinsic thermal resistance can often be approximated as a sum between diffusive and ballistic parts, usually expressed as functions of $K_n$. The diffusive contribution to the thermal resistance will increase with increasing graphene membrane radius and will dominate the resistance for large flakes. In this regime, the graphene radius becomes much larger than the average MFP of phonons ($r \gg l$), therefore, phonon–phonon Umklapp resistive scattering processes become dominant [33, 47] and the heat transport starts to decrease. Note that in relatively large graphene samples the contribution of the $R_b$ to the intrinsic thermal resistance seems to remain a matter of ongoing debate due to the fact that heat transport is significantly affected by the size of the heat source [52–54]. For instance, according to a previous work [54], where a nanometer size heat source was used, an increase of the thermal resistance in relatively large graphene samples was observed taking into account the contribution of the ballistic resistance. Nevertheless, even if the contribution of $R_b$ would be substantial, it will remain constant in the diffusive regime of the membrane conductance and therefore does not conflict with our interpretation.

This behavior reflects the crossover from ballistic to diffusive thermal transport and is visible in our experimental data in graphene discs with a radius larger than 775 nm. Note that this transition has been confirmed also in the second set of measurements (figure S7). We note, that the scaling of the ballistic and diffusive resistance of the graphene and of the interface is not only subject to geometry but a size-dependence of the phonon density of states. The longest phonon wavelength that can support transport is limited by the size of the suspended part of the flake. Low frequency / long wavelength phonons contribute significantly to thermal transport in graphene [49, 55], and therefore the unexpected, almost linear scaling of thermal resistance versus radius in the ballistic regime may be due to both geometry and density of states scaling.

According to a previous work [32], a cross-over from diffusive to quasi-ballistic regime is expected as the suspended CVD graphene length is reduced below 1 μm. However, the experimental data presented by Jo *et al* [32] did not show clear signatures of ballistic thermal transport at room temperature. The identification of ballistic transport features in CVD graphene samples also was neither possible in recent reported heat transport data observed by Xu *et al* [22], either due to the strong scattering of the low-frequency phonons by polymer residue [15, 32] or the limited heat flux resolution. Moreover, the previous works did not provide any information about the morphology and the surface quality of the suspended graphene and the thermal measurements performed with the same experimental method. Note that in the previous studies, the micrometre size heat sources were similar to the length of the suspended graphene, therefore ballistic heat transport was difficult to be revealed.

## 4. Conclusions

In summary, we measured the radius-dependence of the thermal resistance of suspended CVD graphene discs using a high-resolution thermal microscope in a vacuum environment. We found that in suspended graphene discs with a radius smaller than 775 nm, ballistic acoustic phonons dominate the in-plane heat transport and the measured thermal resistance becomes a function of the graphene radius. In graphene discs with a radius larger than 775 nm and without contamination from polymer residues, the in-plane heat transport was suppressed by phonon–phonon scattering and the thermal resistance increased with increasing graphene radius. These results indicated that the value of the average MFP of acoustic phonons in clean suspended graphene that dominate heat conduction at room temperature is approximately 775 nm. Furthermore, our scanning thermal microscope allowed the direct thermal imaging of suspended graphene with spatially resolved heat flux measurements down to few-nanometer spatial resolution by simultaneously analyzing the surface morphology of the graphene samples. We conclude that graphene's surface quality (e.g. defect concentration and surface contaminations) and morphology can have crucial influence on in-plane thermal conductance measurements, and need to be included to extract graphene's intrinsic transport properties. The combination of a high-resolution SThM and suspended materials provide a promising platform to reveal intrinsic heat transport properties of graphene and other 2D material systems.

## Acknowledgments

## Notes

The authors declare no competing financial interest.

## ORCID iDs

A El Sachat ● https://orcid.org/0000-0003-3798-9724
F Alzina ● https://orcid.org/0000-0002-7082-0624

## References

[1] Bolotin K I, Sikes K J, Jiang Z, Klima M, Fudenberg G, Hone J, Kim P and Stormer H L 2008 *Solid State Commun.* **146** 351–5
[2] Balandin A A 2011 *Nat. Mater.* **10** 569
[3] Ghosh S, Calizo I, Teweldebrhan D, Pokatilov E P, Nika D L, Balandin A A, Bao W, Miao F and Lau C N 2008 *Appl. Phys. Lett.* **92** 151911
[4] Pop E, Varshney V and Roy A K 2012 *MRS Bull.* **37** 1273–81
[5] Munoz E, Lu J and Yakobson B I 2010 *Nano Lett.* **10** 1652–6
[6] Saito K, Nakamura J and Natori A 2007 *Phys. Rev.* B **76** 115409
[7] Yamamoto T, Watanabe S and Watanabe K 2004 *Phys. Rev. Lett.* **92** 075502
[8] Park M, Lee S-C and Kim Y-S 2013 *J. Appl. Phys.* **114** 053506
[9] Balandin A A, Ghosh S, Bao W, Calizo I, Teweldebrhan D, Miao F and Lau C N 2008 *Nano Lett.* **8** 902–7
[10] Faugeras C, Faugeras B, Orlita M, Potemski M, Nair R R and Geim A K 2010 *ACS Nano* **4** 1889–92
[11] Cai W, Moore A L, Zhu Y, Li X, Chen S, Shi L and Ruoff R S 2010 *Nano Lett.* **10** 1645–51
[12] Ghosh S, Bao W, Nika D L, Subrina S, Pokatilov E P, Lau C N and Balandin A A 2010 *Nat. Mater.* **9** 555
[13] Lee J-U, Yoon D, Kim H, Lee S W and Cheong H 2011 *Phys. Rev.* B **83** 081419
[14] Chen S *et al* 2011 *ACS Nano* **5** 321–8
[15] Seol J H *et al* 2010 *Science* **328** 213–6
[16] Jang W, Chen Z, Bao W, Lau C N and Dames C 2010 *Nano Lett.* **10** 3909–13
[17] Wang Z, Xie R, Bui C T, Liu D, Ni X, Li B and Thong J T 2011 *Nano Lett.* **11** 113–8
[18] Pettes M T, Jo I, Yao Z and Shi L 2011 *Nano Lett.* **11** 1195–200
[19] Jang W, Bao W, Jing L, Lau C N and Dames C 2013 *Appl. Phys. Lett.* **103** 133102
[20] Wang J, Zhu L, Chen J, Li B and Thong J T L 2013 *Adv. Mater.* **25** 6884–8
[21] Sadeghi M M, Jo I and Shi L 2013 *Proc. Natl Acad. Sci. USA* **110** 16321–6
[22] Xu X *et al* 2014 *Nat. Commun.* **5** 3689
[23] Denis L N and Alexander A B 2017 *Rep. Prog. Phys.* **80** 036502
[24] Denis L N and Alexander A B 2012 *J. Phys.: Condens. Matter* **24** 233203
[25] Deng S and Berry V 2016 *Mater. Today* **19** 197–212
[26] Calado V E, Schneider G F, Theulings A M M G, Dekker C and Vandersypen L M K 2012 *Appl. Phys. Lett.* **101** 103116
[27] Lanza M *et al* 2013 *J. Appl. Phys.* **113** 104301
[28] Wang C, Liu Y, Li L and Tan H 2014 *Nanoscale* **6** 5703–7

[29] Lau C N, Bao W and Velasco J 2012 *Mater. Today* **15** 238–45

[30] Liu N, Pan Z, Fu L, Zhang C, Dai B and Liu Z J N R 2011 *Nano Res.* **4** 996

[31] Pan Z, Liu N, Fu L and Liu Z 2011 *J. Am. Chem. Soc.* **133** 17578–81

[32] Jo I, Pettes M T, Lindsay L, Ou E, Weathers A, Moore A L, Yao Z and Shi L 2015 *AIP Adv.* **5** 053206

[33] Dorgan V E, Behnam A, Conley H J, Bolotin K I and Pop E 2013 *Nano Lett.* **13** 4581–6

[34] Menges F, Riel H, Stemmer A and Gotsmann B 2016 *Rev. Sci. Instrum.* **87** 074902

[35] Hébert C, Masvidal-Codina E, Suarez-Perez A, Calia A B, Piret G, Garcia-Cortadella R, Illa X, Del Corro Garcia E, De la Cruz Sanchez J M and Casals D V 2018 *Adv. Funct. Mater.* **28** 1703976

[36] Ferrari A C 2007 *Solid State Commun.* **143** 47–57

[37] Drechsler U, Bürer N, Despont M, Dürig U, Gotsmann B, Robin F and Vettiger P 2003 *Microelectron. Eng.* **67–8** 397–404

[38] Cerda E and Mahadevan L 2003 *Phys. Rev. Lett.* **90** 074302

[39] Ishigami M, Chen J H, Cullen W G, Fuhrer M S and Williams E D 2007 *Nano Lett.* **7** 1643–8

[40] Chen Z, Jang W, Bao W, Lau C N and Dames C 2009 *Appl. Phys. Lett.* **95** 161910

[41] Kelly B T 1981 *Physics of Graphite* (London: Applied Science)

[42] Bonini N, Garg J and Marzari N 2012 *Nano Lett.* **12** 2673–8

[43] Fugallo G, Cepellotti A, Paulatto L, Lazzeri M, Marzari N and Mauri F 2014 *Nano Lett.* **14** 6109–14

[44] Feng T and Ruan X 2018 *Phys. Rev. B* **97** 045202

[45] Maassen J and Lundstrom M 2015 *J. Appl. Phys.* **117** 035104

[46] Pumarol M E, Rosamond M C, Tovee P, Petty M C, Zeze D A, Falko V and Kolosov O V 2012 *Nano Lett.* **12** 2906–11

[47] Bae M H, Li Z, Aksamija Z, Martin P N, Xiong F, Ong Z Y, Knezevic I and Pop E 2013 *Nat. Commun.* **4** 1734

[48] Mei S, Maurer L N, Aksamija Z and Knezevic I 2014 *J. Appl. Phys.* **116** 164307

[49] Nika D L, Ghosh S, Pokatilov E P and Balandin A A 2009 *Appl. Phys. Lett.* **94** 203103

[50] Puyoo E, Grauby S, Rampnoux J-M, Rouvière E and Dilhaire S 2011 *J. Appl. Phys.* **109** 024302

[51] Prasher R 2005 *Nano Lett.* **5** 2155–9

[52] Chiloyan V, Huberman S, Maznev A A, Nelson K A and Chen G J 2017 (arXiv:1710.01468)

[53] Hoogeboom-Pot K M *et al* 2015 *Proc. Natl Acad. Sci.* **112** 4846–51

[54] Hwang G and Kwon O 2016 *Nanoscale* **8** 5280–90

[55] Sadeghi M M, Pettes M T and Shi L 2012 *Solid State Commun.* **152** 1321–30